UNIVERSITY OF BIRMINGHAM

University of Birmingham
Research at Birmingham

Acoustic waves for active reduction of contact time in droplet impact

H Biroun, Mehdi; Li, Jie; Tao, Ran; Rahmati, Mohammad; Mchale, Glen; Dong, Linxi; Jangi, Mehdi; Torun, Hamdi; Fu, Yongqing

Document Version
Publisher's PDF, also known as Version of record

[Link to publication on Research at Birmingham portal](#)

Acoustic Waves for Active Reduction of Contact Time in Droplet Impact

Mehdi H. Biroun[1], Jie Li[2], Ran Tao[1,3], Mohammad Rahmati[1], Glen McHale[1], Linxi Dong[2], Mehdi Jangi[4], Hamdi Torun[1], and YongQing Fu[1,*]

[1]*Faculty of Engineering & Environment, Northumbria University, Newcastle upon Tyne NE1 8ST, United Kingdom*

[2]*Smart Microsensors and Microsystems Engineering Research Center of Ministry of Education, College of Electronics and Information, Hangzhou Dianzi University, Hangzhou 310018, China*

[3]*Shenzhen Key Laboratory of Advanced Thin Films and Applications, College of Physics and Optoelectronic Engineering, Shenzhen University, Shenzhen 518060, China*

[4]*Department of Mechanical Engineering, University of Birmingham, Birmingham B15 2TT, United Kingdom*

Minimizing droplet impact contact time is critical for applications such as self-cleaning, antierosion or anti-icing. Recent studies have used the texturing of surfaces to split droplets during impact or inducing asymmetric spreading, but these require specifically designed substrates that cannot be easily reconfigured. A key challenge is to realize an effective reduction in contact time during droplet impingement on a smooth surface without texturing but with active and programmable control. Our experimental results show that surface acoustic waves (SAWs), generated at a location distant from a point of droplet impact, can be used to minimize contact time by as much as 35% without requiring a textured surface. Additionally, the ability to switch on and off the SAWs means that a reduction in droplet impact contact time on a surface can be controlled in a programmable manner. Moreover, our results show that, by applying acoustic waves, the impact regime of the droplet on the solid surface can be changed from deposition or partial rebound to complete rebound. To study the dynamics of droplet impact, we develop a numerical model for multiphase flow and simulate different droplet impingement scenarios. Numerical results reveal that the acoustic waves can be used to modify and control the internal velocity fields inside the droplet. By breaking the symmetry of the internal recirculation patterns inside the droplet, the kinetic energy recovered from interfacial energy during the retraction process is increased, and the droplet can be fully separated from the surface with a much shorter contact time. Our work opens up opportunities to use SAW devices to minimize the contact time, change the droplet impact regime, and program or control the droplet's rebounding on smooth or planar and curved surfaces, as well as rough or textured surfaces.

I. INTRODUCTION

Water-repellent materials and surfaces are widespread among plants and animals, such as rice and lotus leaves, mosquito eyes, spider silks, fish scales, and red rose petals [1,2]. They inspire researchers to develop different biomimetic surfaces with nonwettability for various applications, such as self-cleaning, liquid collection, anticorrosion, antifogging, drag reduction, antierosion, anti-icing, and deicing [3–6].

A droplet bouncing onto a solid water-repellent surface will spread out onto the surface to a maximum contact diameter [7,8] and then retract until it partially wets or completely rebounds and detaches from the surface [9,10]. In this case, surface features such as texture and hydrophobicity play key roles in determining the rebounding shapes,

patterns, and contact time. The period that the droplet is in contact with the solid surface depends on the droplet inertia, capillary forces, volume of the droplet, surface texture or topography, and solid-liquid interaction during spreading and retracting [11]. It is well known that droplet contact time is dominated by the retraction phase, rather than spreading phase [12], and is limited by the Rayleigh limit for symmetrical rebounding [13].

To reduce the droplet retraction time, many studies are focused on changing the symmetrical shape of the droplet during impingement. A droplet can be split during impact by a submillimeter ridge or blade on the surface, thus leading to contact-time reduction. Bird *et al.* [14] showed that the symmetry of a droplet impinging on a single ridge on a surface would break and the contact time could be significantly reduced. To do this, they designed a structure with a single ridge and achieved a shorter contact time. Later, Gauthier *et al.* [15] showed that the droplet contact time on ridged macrostructures took discrete values when the

impact speed was varied. They discussed that, depending on impact velocity, a different number of lobes could be shaped during the spreading phase, and the contact time could be reduced by the square root of the number of the lobes. They also designed a Y-shaped ridge on the smooth solid surface to break the droplet into three subunits and found that the contact time (when the droplet impacted onto the center of the Y shape) was reduced by a factor of $\sqrt{3}$. Similarly, Shen *et al.* [16] demonstrated that, by impacting the water droplet onto cross-shaped blades on the surface, the retraction phase could be merged into the spreading one, and a limited contact time of 5.5 ms could be achieved. Recently, Li *et al.* [17] showed that, by patterning surface wettability, translational motion during retraction could be converted to gyration, thereby creating a rotational rebound.

Although the aforementioned methods can decrease the contact time, they are only effective when droplets impact on a certain point on the surface along a certain direction, which presents challenges for their translation into real-world applications. To overcome this issue, different types of macrostructures have been introduced in the literature to reduce the contact time on a larger contact area. A group of researchers focused on the fabrication of macrogrooves on solid surfaces to break the droplet symmetry and change the impact behavior [11,18–22]. For example, Song *et al.* [21] designed and fabricated an anisotropic grooved surface and were able to reduce the contact time by about 45% when the distance between the grooves was comparable to the droplet diameter. Recently, Guo *et al.* [22] showed that a droplet impacting on a grooved surface within a certain range of impact velocity could be detached from the surface in a petal-like shape, leading to a reduction in contact time of 70%. Abolghasemibizaki and Mohammadi [11] studied a droplet's impact on a superhydrophobic surface with cylindrical macrostructures and showed that the retraction time was decreased by the factor of about $\sqrt{2/\pi}$.

Macrostructured surfaces with designs of different post-shaped arrays are also used to reduce the contact time of bouncing droplets [4,23,24]. For example, Liu *et al.* [25,26] showed that a droplet would be spread on a surface patterned with arrays of submillimeter truncated pyramidal postshaped arrays and detached from the surface in a pancake shape, leading to a contact-time reduction of up to about 50%. Later, Song *et al.* [27] studied the effect of the size of pillar arrays and introduced a manufacturing method of the superhydrophobic pillar arrays over a large area for pancake bouncing.

Another approach to decrease the contact time is droplet impact on curved smooth surfaces. The droplet symmetry can also be altered by impacting on cylindrically curved surfaces [28–30]. For example, Liu *et al.* [28] numerically and experimentally investigated droplet impact on convex-concave surfaces. Their results showed that asymmetric momentum distribution during impact led to about

40% reduction in contact time compared with that on a flat surface.

In addition to efforts to decrease the contact time by changing the solid surface's texture and geometry, active methods, such as vibrating the solid surface, are used. Weisensee *et al.* [31] investigated the effect of the vibration of a solid surface at frequencies of 60–320 Hz and amplitudes of 0.2–2.7 mm during droplet impact. Their results showed that, by vibrating the solid surface at frequencies higher than 100 Hz, the contact time could be decreased by 50%.

The need for manufacturing a textured surface with macrostructures or vibrating whole structures brings complexity, especially at a large scale for practical applications. It is, therefore, crucial to find alternative methodologies to manipulate droplet impact on a smooth and nontextured surface with large-area coverage. Here, we hypothesize that the contact time of an impacting droplet may be reduced by remotely generating surface acoustic waves (SAWs), which then propagate along a smooth and nontextured surface into the area where droplet impact is occurring. For the experimental investigation, we design and fabricate thin-film SAW devices to apply wave energy to the droplet during its impingement process. We discover that it is possible to reduce the contact time by up to 35% by applying a SAW along one side of the droplet, whereas the reduction is only about 10% when the SAW is applied along two opposing directions with the same amplitude. Furthermore, results show that the droplet impact regime can be effectively changed from droplet deposition on the surface to fully rebounding by using SAWs. Using these insights, droplet impingement properties, such as contact time and rebounding angle, can be programmed and controlled electrically.

To understand the underlying physics of these phenomena, we develop a numerical method and simulate the droplet impact process with and without SAW actuation. After validation of the method with experimental results, we compare the numerical results for different scenarios of droplet impact. High-fidelity numerical results show that there are apparent differences in internal streaming patterns of the droplet during impact, which lead to higher kinetic energy, vertical momentum, and less-viscous dissipation inside the droplet subjected to SAW power that is driven from one side, compared with those for the droplet driven from both sides. As a result, the droplet is separated from the surface slightly slower in the latter case.

II. DESIGN AND THEORETICAL ANALYSIS

SAW-based microfluidics (acoustofluidics) has recently found many applications in lab-on-a-chip [32–34] tissue engineering [35], biology, and medicine [36–38]. SAWs can be generated by applying a radiofrequency (rf) signal to interdigital transducers (IDTs) that are patterned

on a piezoelectric substrate. When the propagating SAWs reach a liquid medium on the substrate, depending on their amplitudes and frequencies, as well as the properties of the liquid and piezoelectric substrate material, their momentum is transferred inside the liquid along the Rayleigh angle ($\theta_R = \sin^{-1} v_L/v_S$, where v_L and v_S are the sound velocity in liquid and solid media, respectively) [39]. Different droplet actuation phenomena, as a result of the transferred momentum, including mixing, pumping, jetting, and atomization, by the SAW have been extensively investigated over the last two decades [39]. The generation of leaky SAWs at the interface of liquid and solid surfaces affects internal streaming patterns inside an impinging droplet, and thus, can lead to breaking of the symmetry of patterns and result in a potential reduction of the droplet impact time. The momentum transferred by a SAW to a droplet can be described using a body force, which is applied to the liquid medium along the Rayleigh angle, by [40,41]

$$F_{\text{SAW}} = -\rho(1 + \alpha_1^2)^{3/2} A^2 \omega^2 k \cdot \exp[2(kx + \alpha_1 kz)], \quad (1)$$

where A and ω are the wave amplitude and frequency, respectively; k is the imaginary part of k_L, which is the wave number of leaky surface acoustic waves (LSAWs). $\alpha_1 = \sqrt{(v_S/v_L)^2 - 1}$ is the attenuation constant. Figure 1 illustrates the droplet impingement dynamics on the solid surface in the presence of a propagating SAW. The droplet contact width is characterized by $\beta = \delta/D_0$, which is the ratio of the contact width, δ, to the initial droplet diameter, D_0. We expect to observe droplet interface asymmetry along the x axis, which will be triggered by the conversion of SAW energy into LSAWs and the resulting different internal streaming patterns inside the droplet. This will affect the various interfaces, which, in turn, can lead to different contact widths and dynamics during impingement. It is reasonable to conjecture that the droplet may detach from the surface sooner and along a non-normal detachment angle, as shown in Fig. 1.

Based on the above hypothesis, in this study, we aim to determine whether the contact time will be reduced by applying the SAW during droplet impact on the solid surface. To achieve this, we use a thin-film ZnO/Si SAW device with a resonant frequency of 66.2 MHz. We use two types of designs in this study: (1) traveling surface acoustic waves (TSAWs, i.e., with waves propagating from IDTs along one side of the droplet), and (2) standing surface acoustic waves (SSAWs, i.e., two waves propagating from IDTs along the two opposite sides of the droplet) during droplet impingement. The experimental results are compared with the conventional droplet free impact (DFI) on the solid surface, in terms of contact width and contact time as functions of SAW amplitude and the Weber number (We = $\rho U_0^2 D_0/\gamma$, in which ρ, U_0, D_0, and γ are
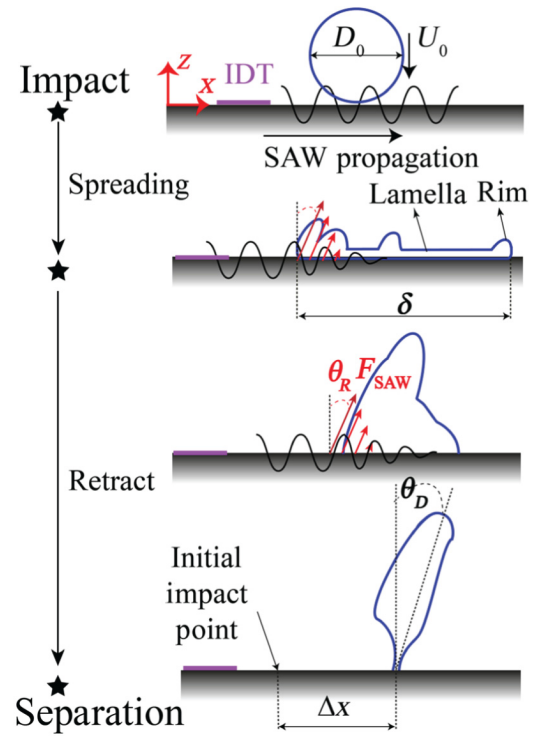

FIG. 1. Anticipated time evolution of droplet impact on a solid surface in the presence of SAWs propagating on the surface. SAWs can dissipate energy into the liquid droplet during the impact process and break the symmetry in a droplet spreading and the retracting phase, leading to shorter contact time.

the density, impact velocity, initial diameter, and surface tension of the droplet, respectively).

III. MATERIALS AND METHODS

A. SAW device preparation

ZnO films with a thickness of 5 μm are deposited onto (100) silicon wafers and aluminum plates using a direct-current magnetron sputter system (NS3750, Nordiko). The vacuum of the sputter chamber is maintained at about 0.35 Pa during deposition, with an Ar/O$_2$ flow ratio of 3:11. The Cr/Au IDTs, with a thickness of 20/100 nm, are fabricated on the ZnO/Si and ZnO/Al substrate using a standard photolithography and lift-off process. The bidirectional IDTs consist of 30 pairs of fingers, with an aperture of 5 mm and spatial periodicities of 36–200 μm. To obtain a hydrophobic surface, the surface of the SAW device is coated with a hydrophobic CYTOP™ (Asahi Glass Co.) layer. To measure the resonant frequency and the amplitude of the SAW device, an HP8752A rf network analyzer is used. The Rayleigh wave generated by a signal generator (Marconi 2024, Plainview, USA) is amplified using an rf power amplifier (Amplifier research, 75A250, Souderton, USA) before applying it to the IDTs. The measured resonant frequencies of the fabricated ZnO/Si SAW devices

TABLE I.　Resonant frequency, Rayleigh angle, contact time (CT), static contact angle (SCA), advancing contact angle (ACA), receding contact angle (RCA), and contact-angle hysteresis (CAH) for the ZnO/Si SAW device with and without surface treatment. Standard error is indicated by the $\pm$ sign.

SAW device	Resonant frequency (MHz)	Rayleigh angle (deg)	α_1	θ_s (deg)	θ_{adv} (deg)	θ_{rec} (deg)	$\Delta\theta = \theta_{adv} - \theta_{rec}$ (deg)
CYTOP/ZnO/Si	66.1	21.2	2.47	122 ± 2	123 ± 2	95 ± 4	28 ± 6
ZnO/Si				86 ± 3	90 ± 4	27 ± 4	63 ± 8

and calculated velocities are listed in Table I. To convert the applied power to the nondimensional SAW amplitude, the equation proposed by Alghane *et al.* is applied [42]:

$$\frac{A}{\lambda} = 8.15 \times 10^{-6} P_{rf}^{0.225} + 5 \times 10^{-6} P_{rf}^{0.8}, \qquad (2)$$

where λ is the wavelength of the SAW in m, and P_{rf} is the power applied to the SAW device in W.

B. Droplet bouncing and imaging

Droplets of deionized water, with a density of $\rho = 995 \ kg \ m^{-3}$ and surface tension $\gamma_{LV} = 72 \times 10^{-3} \ Nm^{-1}$ at 21 °C, with volumes between 3.56 and 5.84 μl are generated by squeezing the nozzle until the droplet is detached under gravity from the edge of a needle (BD Microlance). For each needle, the droplet size is calculated using the approach proposed by Aminzadeh *et al.* [43] and is repeatable within <5%. By adjusting the drop height, the impact velocity is varied between 1.4 and 2 m/s. The impact process is filmed in side view using a high-speed Camera (HotShot 1280CC) at 5000 fps. Droplet contact time, τ, is defined for all cases between the first touch of the droplet to the surface and when the water is separated from the substrate. The SAW is applied just before droplet detachment from the needle to avoid a temperature rise in the solid surface. The temperature of the surface is maintained at room temperature (21 °C) in all cases. Each impact is repeated three times to ensure the repeatability of the experiment. Table I lists the measured data for the SAW devices.

C. Numerical method

To numerically investigate the impact cases, an interface capturing method based on the coupled level-set volume of fluid (CLSVOF) method is developed using an Open-FOAM 4.x. open-source toolbox. The CLSVOF method is used to capture a sharp and smooth liquid-gas interface and conserve the mass during calculations [44,45]. The developed code is capable of 3D simulation of unsteady droplet interaction with the solid surface in the presence of SAWs. To optimize the computational costs, the impact is simulated for three different mesh domains. The droplet is released from a height of 10 cm from the surface, which is simulated by a rectangular mesh with dimensions of $3.2 \times 3.2 \times 102.0 \ mm^3$, consisting of 3 525 120 hexahedral cells. Then the computational fields after 150 ms

are mapped to a new rectangular mesh with a dimension of $7.0 \times 7.0 \times 3.0 \ mm^3$, consisting of 3 786 444 hexahedral cells, to simulate the spreading and retracting phases. Finally, to simulate the detachment phase, another rectangular domain with dimensions of $3.0 \times 3.0 \times 6.0 \ mm^3$, consisting of 3 456 000 hexahedral cells, is used. The mesh resolution of the drop is 35 cells per diameter. Variable time steps with a maximum Courant number of 0.3 are chosen to keep the normalized residuals below 10^{-5}. A dynamic-contact-angle model is developed to capture the spreading and retracting dynamics accurately [see Eq. (7) in Appendix D]. A partial slip velocity boundary condition, based on the model reported by Afkhami *et al.* [46], is developed and used for the solid surface.

IV. RESULTS

A. Experimental results

As explained in Sec. III, different SAW devices on different substrates with resonant frequencies ranging from 22.04 to 110.84 MHz are designed and fabricated to investigate the droplet impact hydrodynamics in the presence of SAWs. Effects of SAW device substrate (i.e., on the generation of different Rayleigh angles) and IDT design (i.e., achieving different resonant frequencies) are shown in Appendixes A and B, respectively. Based on these results, we select the ZnO/Si SAW device with a resonant frequency of 66.10 MHz for further studies. Figures 2(a)–2(c) show snapshots of the droplet impact images on the SAW device surface with CYTOP surface treatment for three different cases of DFI, TSAW, and SSAW, respectively. When the droplet impinges on the solid surface in the cases of DFI and SSAW, it starts to spread to its maximum diameter before it starts to retract, and both deformation patterns are quite symmetrical with respect to the z axis. On the other hand, the TSAW shows a more irregular and asymmetric pattern [see Fig. 2(b)], which is more significant during its maximum spreading and retraction or detachment periods. Figure 3(a) shows comparisons between experimental and simulation results as a function of the normalized contact width for all three impact cases. During the spreading and retracting stages (e.g., $t < 6$ ms), the dynamics are comparable for these three cases. The spreading time (τ_s) for all cases is similar and can be given as $\tau_s/\tau \sim We^{-0.5}$ [47]. The contact time for the TSAW case is reduced by about
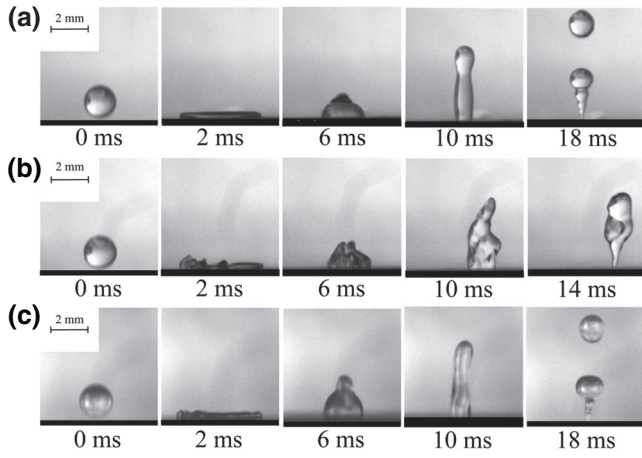
FIG. 2. Experimental snapshots of a water droplet impinging on the solid surface. (a) Droplet free impact case without application of SAWs, (b) impact on ZnO/Si surface with TSAWs applied to propagate from left to right, and (c) impact on ZnO/Si surface while SSAWs are applied to the surface. For all experiments, the droplet impact velocity and volume are 1.4 m/s and 3.56 μl, respectively. See Videos S1–S3 within the Supplemental Material [62] for experimental movies.

4.6 ms compared with the DFI case, mainly due to shortening of the detachment period in this case. Figure 3(b) shows the maximum contact width for both the TSAW and SSAW cases at different SAW amplitudes (i.e., different rf powers applied to the IDTs). By increasing the SAW amplitude, the maximum spreading diameter is decreased. As expected, this radius reduction during impact is higher for the SSAW case, as the x component of the SAW force from both directions restrains contact line movement during the spreading phase.

Figure 3(c) shows the normalized contact time of the droplet versus SAW amplitude. For the TSAW cases, the contact time is reduced by increasing the SAW amplitude. At lower SAW amplitudes ($A/\lambda < 3 \times 10^{-5}$), the reduction percentage of the contact time is not significant, due to the lower energy transferred from the solid surface during impingement. By increasing the normalized SAW amplitude up to 1.2×10^{-4}, the contact time is significantly reduced by about 25%. For the SSAW case, the evolution of the contact time can be divided into two stages. The contact-time reduction is observed at normalized amplitudes lower than 7×10^{-5}, whereas the contact time is increased at normalized amplitudes higher than this value.

The contact time for the DFI scenarios is not a function of impact velocity [48,49]. Interestingly, our experimental results show that there is a threshold of droplet impact velocity for a complete rebound from the hydrophobic and nontextured surface. As shown in Fig. 3(d), with impact velocities lower than 1.26 m/s, the initial kinetic energy of the droplet is not high enough to detach the whole droplet from the surface at the end of the retraction phase. Video S1 within the Supplemental Material [62] shows a rebound case with an impact velocity of 1.4 m/s, and Video S4 shows a deposition case with an impact velocity of 1.08 m/s. The results in Fig. 3(d) show that, by applying the TSAW, the impact regime can be effectively changed from deposition to rebounding for impact velocities lower than 1.26 m/s. Furthermore, for higher impact velocities, applying the TSAW can reduce the contact time by about 25%, on average. The results in Fig. 3(d) indicate that the contact
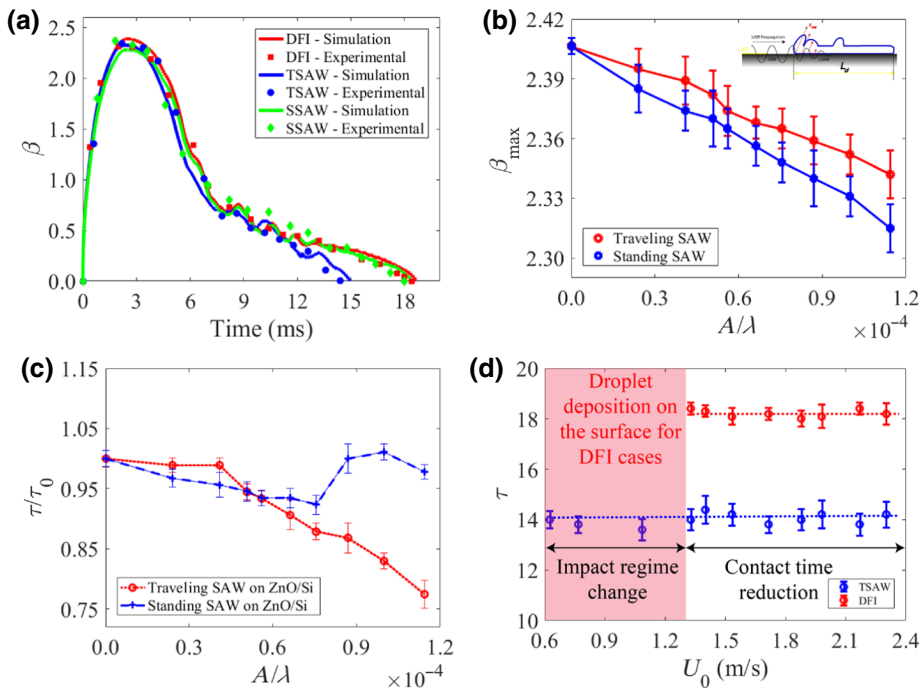
FIG. 3. (a) Comparison between numerical and experimental results for normalized contact widths of droplet impact on SAW device for DFI, TSAW, and SSAW scenarios. (b) Maximum contact width versus SAW amplitude for both SSAW and TSAW cases. Impact experiments are carried out for a droplet with a volume of 3.56 μl and an impact velocity of 1.4 m/s. (c) Normalized contact time as a function of SAW amplitude for a droplet with a volume of 3.56 μl and impact velocity of 1.4 m/s impacting on the ZnO/Si SAW device surface with CYTOP surface treatment. (d) Contact time versus impact velocity for a droplet with a volume of 3.56 μl for DFI and TSAW scenarios. Shaded area represents droplet deposition on the surface for DFI cases. Error bars represent SD of the results.

time of the droplet, regardless of the presence of the SAW, is not a function of impact velocity. The results in Fig. 3(d) show that the TSAW can change the nature of the untextured hydrophobic surface into a water-repellent surface. The effect of the droplet volume on the impact behavior is presented in Appendix C.

To investigate effects of surface treatment and wettability on the impact dynamics, droplet impact tests with a volume of 3.56 μl and an impact velocity of 1.08 m/s are carried out on surfaces with and without CYTOP treatments. The same experiments are repeated in the presence of TSAWs with a normalized amplitude of about 8.7×10^{-5} (i.e., rf power of 27 W applied to the IDTs) for both types of SAW devices. The differences in contact angles of the devices after the surface treatments are listed in Table I.

During the motion of the three-phase contact line (TPCL) on the solid surface, CAH ($\theta_{adv} - \theta_{rec}$),generates a force that resists droplet motion and dissipates the kinetic energy of the droplet. To explain the effect of contact angles on droplet impact hydrodynamics, we focus on analyzing the work done by this resistive force, W_R, which can be written as [49,50]

$$W_R \propto \frac{\cos\theta_{rec} - \cos\theta_{adv}}{1 - \cos\theta_{adv}}. \quad (3)$$

Equation (3) shows that, during impact, a higher ACA or a lower CAH can lead to a lower energy dissipation during the TPCL motion.

For the DFI case, due to large work generated by the resistive force on the surface without hydrophobic treatment, the droplet stays on the surface after impact. In the same DFI case, by treating the surface of the device with a layer of CYTOP, the CAH is decreased by about 35°, while the ACA is increased by about 35°, thus resulting in a reduction of resistance work by 320%. Thus, a much lower value of kinetic energy loss by the CAH resistive force can be expected for the CYTOP-coated surfaces, and partial rebounding of the droplet is observed for the DFI cases on these surfaces (see Videos S4 and S5 within the Supplemental Material [62] and the experimental snapshots shown in Fig. 4). Due to the lower energy dissipation by the CAH resistance work, a subunit of the liquid has enough energy at the end of the retraction phase to overcome surface tension and is separated from the droplet, while the bulk droplet still remains on the surface.

However, for both treated and nontreated surfaces, by applying the TSAW, the droplet gains enough kinetic energy during impingement to bounce off the surface, mainly due to the large vertical SAW momentum dissipated into the liquid by the z component of the SAW force (see Videos S6 and S7 within the Supplemental Material [62] and TSAW experimental snapshots in Fig. 4). As shown in Fig. 4, in the absence of SAWs, the droplet stays
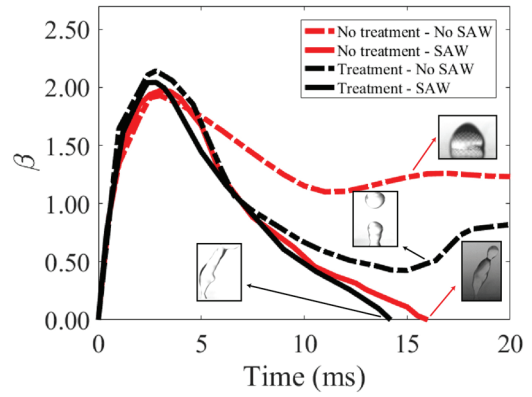

FIG. 4. Temporal evolution of contact width for droplets impacting on the SAW device surface with different wettability. In these experiments, droplet volume and impact velocity are kept constant at 3.56 μl and 1.08 m/s, respectively. For each surface coating, experiments are carried out for both DFI and TSAW scenarios. Applied rf power to the IDTs for the TSAW scenario is 27 W. Snapshots of the experimental results confirm that TSAW changes droplet deposition (red dashed line) and breakup (black dashed line) on the surface to complete rebound (solid lines).

on the surface at the end of the retraction phase. However, by applying the SAW, the droplet gains more energy during impingement and is fully separated from the surface. Due to the lower energy loss induced by the resistive work for the surface with CYTOP coating, less kinetic energy is dissipated, and thus, leads to a faster detachment of the droplet from the surface. Figure 4 shows that, regardless of the surface treatment, applying a TSAW can significantly reduce the contact time. Moreover, the droplet-impact regime can be changed from deposition on the surface to complete rebounding from the surface after applying the SAW.

B. Numerical simulations

To gain a better insight into the physics of contact reduction by the SAW and to interpret the differences of droplet detachment for both the TSAW and SSAW cases, we further analyze the effect of the SAW on the impingement dynamics using numerical simulations. An interface-capturing method based on the CLSVOF method is developed in the OpenFOAM 4.x. open-source toolbox and is used to capture a sharp and smooth liquid-gas interface and conserve the mass during calculations [51,52]. A series of validation simulations are performed to reproduce the experimental results and test the capability of the developed numerical method. Agreement between the experimental and simulation results is achieved, which can be seen from the results shown in Fig. 3(a). More details about the numerical method can be found in Appendix D. For the simulation results, we focus on the internal streaming patterns inside the droplet during its spreading and retraction stages to understand the mechanism by which
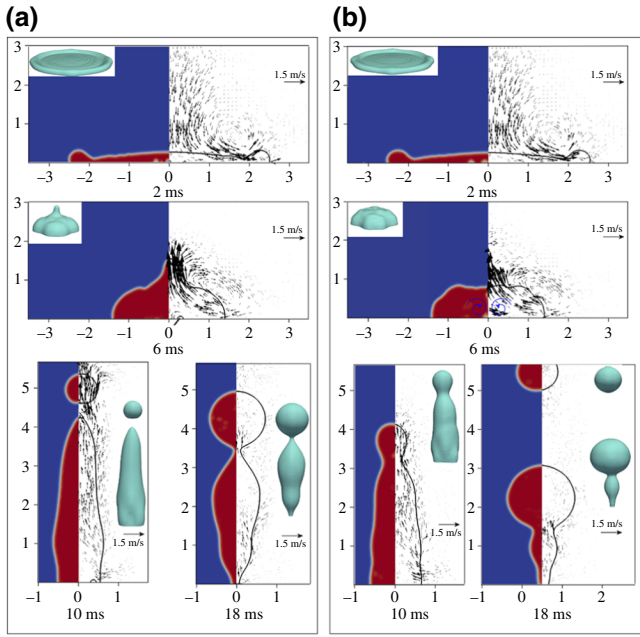
FIG. 5. Time-evolution images of droplet impact dynamics obtained by numerical simulation. (a) DFI scenario. (b) SSAW propagation on the solid surface during impact. In all simulations, droplet impact velocity and volume are 1.4 m/s and 3.56 μl, respectively.

different SAW modes change the contact time. As observed in Fig. 5, while the velocity vectors for the DFI and SSAW cases demonstrate rather regular and symmetric flow patterns, the results for the TSAW case (see Fig. 6) involve an irregular flow pattern and a strong internal recirculation on the left-hand side.

As the process evolves over time, relatively regular flow patterns for both DFI and SSAW cases are developed. It is worth mentioning that both the DFI and SSAW cases exhibit very similar spreading flow patterns with an almost identical maximum spreading diameter of 2.4 mm, while the apparent differences between these two cases are only observed at a much later stage, e.g., after 6 ms, which is during the retraction period. The case for the TSAW, however, shows very different behavior. Considering the shape of the interface in Fig. 6 at a time of 3 ms, we notice the initiation of an asymmetric deformation at the interface near the rim in the left-hand side (where it is subjected to SAWs). This deformation is not present on the right-hand side of this case, nor can it be found in the results for DFI and SSAW cases. The same asymmetric deformation can be seen in Fig. 2(b). This irregular deformation at the droplet interface, which is initially triggered by the one-sided SAW at 2.5 ms during the spreading period, is rapidly developed during the retraction phase of droplet impact. The asymmetric retraction of the droplet, in turn, creates even more irregular deformations and instabilities at the interface and rapidly develops an asymmetric flow
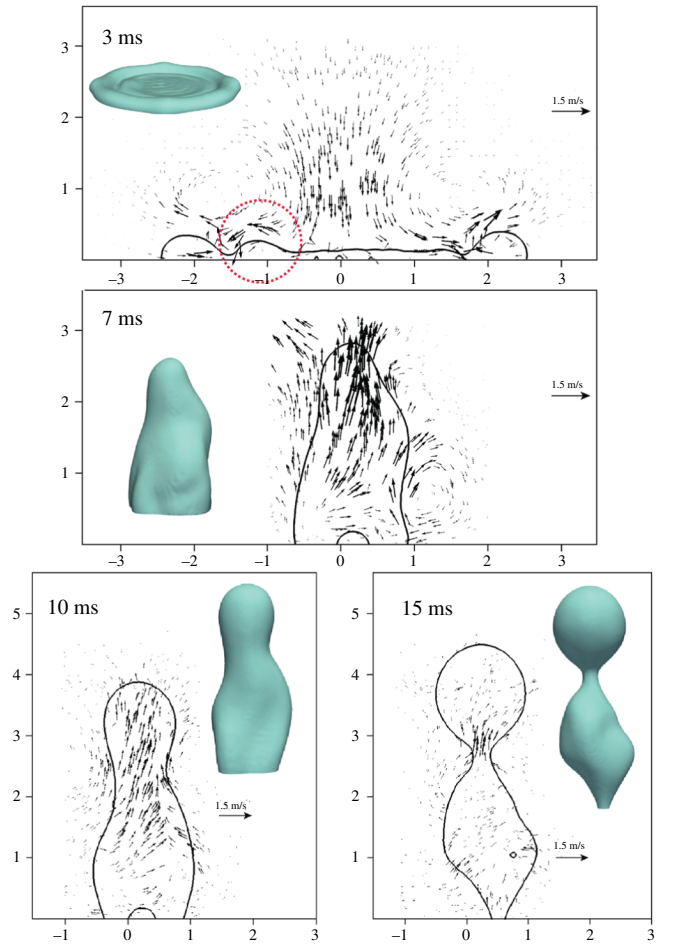

FIG. 6. CFD snapshots of liquid phase overlaid by velocity vectors during impingement process in the presence of TSAWs propagating from left to right. Droplet impact velocity and volume are 1.4 m/s and 3.56 μl, respectively.

pattern with a dissimilar interface morphology, as observed in Fig. 6 after 7 ms.

During the impingement process, there are continuous changes of gravitational, kinetic, and liquid-vapor-solid interfacial and surface energies. Furthermore, these energies are continuously dissipated during impact because of viscous dissipation, wave generation on the interface, and subunit separation [53,54]. We further analyzed the energy budget and the rates of conversion of the initial energy of the droplet, E_0, into the kinetic energy, potential energy, and interfacial energy to reveal the real mechanism of contact-time reduction in the TSAW case. The total interfacial or surface energy of the solid-liquid-vapor system (E_{interf}) for a droplet in contact with the substrate can be given by

$$E_{\mathrm{interf}} = \gamma_{\mathrm{LV}} S_a + (\gamma_{\mathrm{SL}} - \gamma_{\mathrm{SV}}) S_s + \gamma_{\mathrm{SV}} S_\infty, \quad (4)$$

where γ_{SV}, γ_{SL}, and γ_{LV} are the interfacial tensions (i.e., surface energies per unit area) of the solid-vapor, solid-liquid, and liquid-vapor interfaces, respectively. S_a and S_s are the areas of the droplet interfaces in contact with air and solid, respectively, and S_∞ is the area of the solid surface in contact with the gas phase in the absence of a droplet. Here, the changes in interfacial energy associated with droplet spreading can be defined as $E_D = E_{\mathrm{interf}} - \gamma_{SV}S_\infty$, which sets the reference interfacial energy, E_D, equal to the droplet surface energy at the instant of droplet impact on the surface.

We define the sum of the kinetic, E_K; gravitational, E_G; and interfacial energy associated with droplet spreading, E_D, as the total energy of the droplet:

$$E = E_K + E_G + E_D, \tag{5}$$

where E_G is defined as the volume integral of the infinitesimal volume element V potential energy through the liquid phase

$$E_G = \int \rho_l g z dV, \tag{6}$$

where g is the gravitational acceleration, ρ_l is the liquid density, and z is the distance in the vertical direction from the solid surface. The kinetic energy E_K is defined as

$$E_K = \int \frac{1}{2}\rho_l u^2 dV, \tag{7}$$

where u is the magnitude of the liquid velocity. The time evolution of the energies during the impingement process is shown in Fig. 7. All energies are normalized by the initial droplet total energy, $E_0 = (\rho_l V_0 g H_0 + \gamma_{LV}S_0)$, where H_0, S_0, and V_0 are the droplet's initial release height, spherical surface area, and volume, respectively.

The normalized total energy of the droplet during impingement, E/E_0, is illustrated in Fig. 7(a). Interestingly, more than 70% of the total energy is dissipated within less than 0.5 ms after the onset of impact, which is consistent with the findings in Refs. [53,55,56]. Since the potential energy is one order of magnitude smaller than that of the kinetic and interfacial energies in Eq. (5), it is not shown in Fig. 7.

The variation of kinetic energy, E_K (normalized by E_0), shown in Fig. 7(b), indicates its significant reduction in the first 0.5 ms of the impact time. The results in Fig. 7(c) show that only 10% of the kinetic energy is stored in the form of interfacial energy during the spreading phase, and the rest of the kinetic energy is dissipated during the first 0.5 ms of impact. The stored interfacial energy at the end of the spreading phase starts to be converted into kinetic energy and causes retraction. The conversion of interfacial energy into kinetic energy leads to an increase in kinetic energy between 3 and 6 ms after the onset of impact. This increase in kinetic energy is more significant for the TSAW scenario, since the kinetic energy is increased by both interfacial energy conversion and applied SAW energy. However, for the SSAT and DFI scenarios, due to the symmetry of droplet deformation, a rather strong internal recirculation field is created within the droplet, which dissipates the kinetic energy.

More importantly, Figs. 7(a)–(c) show that the energy conversion rates for all cases during the spreading and
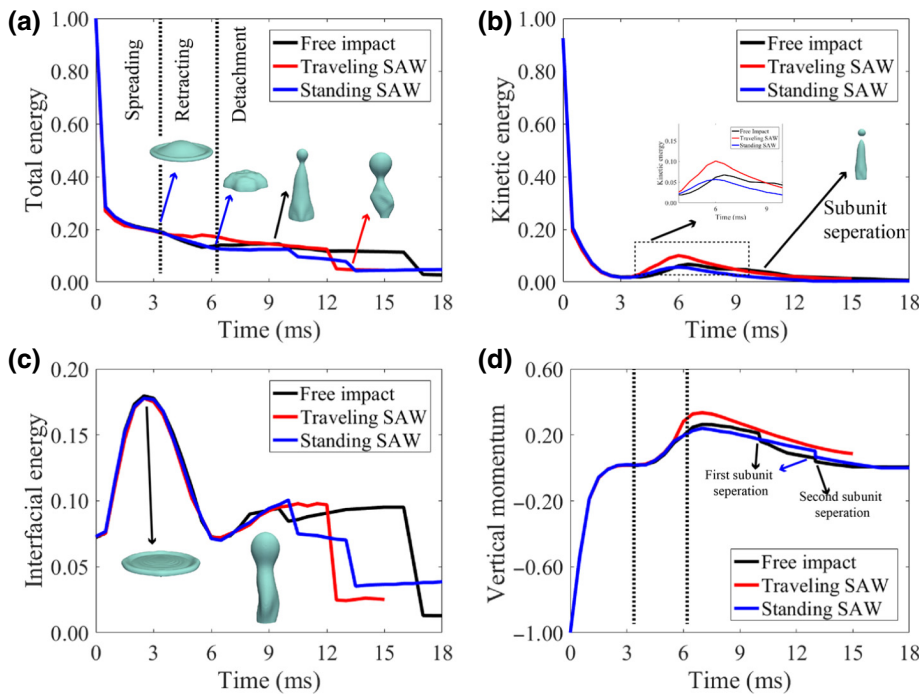

FIG. 7. (a) Total energy, (b) kinetic energy, and (c) interfacial energy for FI, TSAW, and SSAW scenarios. In the simulation, droplet impact velocity and volume are 1.4 m/s and 3.56 μl, respectively. All energies are normalized by kinetic energy at the onset of impact. (d) Droplet vertical momentum normalized by the vertical momentum at the onset of the impact.

retracting time, e.g., <6 ms, are almost identical. This implies that dissipation of the total initial energy by a viscous liquid and the interaction between liquid and solid surfaces are the two dominant processes during the initial 6 ms. However, the differences between these cases begin to appear in the values of kinetic energy, after approximately 3.5 ms, because of the presence of the SAW, which is shown in the inset in Fig. 7(b). For example, the recovery rate of the kinetic energy from the interfacial energy between 3.5 and 6 ms is about 37% higher for the TSAW case than that of the SSAW case. The normalized vertical momentum of the droplet by the initial droplet momentum is shown in Fig. 7(d). The differences in kinetic energy, in turn, increase the vertical momentum of the droplet during the retraction phase. Also, the separation of each subunit from the main droplet leads to a sudden decrease in momentum, which delays droplet detachment from the surface.

Another interesting phenomenon obtained from Fig. 7(c) is that, while apparent differences of the variation of kinetic energy between TSAW with those of SSAW and DFI are observed, the interfacial energy in all cases is almost identical during the spreading and retraction phases. This clearly shows that the dissipation rate for the TSAW case during the retraction period is 50% smaller than those of SSAW and DFI cases. Snapshots in shown in Figs. 5(a) and 5(b) reveal the mechanism responsible for such higher dissipation rates in the cases of SSAW and DFI. It can be seen in Figs. 5(a) and 5(b) at 6 ms that rather symmetric small-scale vortices form for both SSAW and DFI cases. Such small-scale vortices do not form in the TSAW case due to its asymmetric and irregular flow patterns. It is well known that the viscous dissipation rate is exponentially proportional to the inverse of the vortex length scale [57]. Therefore, the conversion of interfacial energy during the retraction period for the TSAW case occurs with a much lower dissipation rate, owing to the absence of such vortices, which, in turn, leads to a much higher energy-conversion efficiency and much larger kinetic energy and vertical momentum inside the droplet during the retraction phase.

All of the above results indicate that most energies in the SSAW and DFI cases during the retraction processes are dissipated by symmetric and very stable internal flow recirculation. On the other hand, they are recovered as kinetic energy more efficiently in the TSAW case, since such internal recirculation cannot be easily formed due to the asymmetric shape and instabilities. This, in turn, leads to much faster retraction and dispatching processes of the droplet from the surface in the TSAW case. Simulation results show that, by increasing asymmetry in the flow inside the liquid, a shorter contact time can be achieved during droplet impact under the TSAWs.

To further verify this idea, we examine the droplet impact dynamics using a sample with a perpendicular IDT design, which can generate two waves propagating in vertical directions into the droplets (see Fig. 8). Three different cases are tested, and the results are illustrated in Fig. 8(a). Depending on the droplet size, the contact time can be reduced by between 20 and 35%, if compared with the DFI case. Unlike the SSAW cases, in this IDT design, the applied SAWs from both sides create a kinetic energy field that breaks the symmetry of droplet deformation in both x and y directions and speed up the detachment process of the bouncing droplet. Figure 8(b) shows the effects of the impact velocity for the droplet impact dynamics. At lower SAW amplitudes, the contact times for all cases do not show significant differences. However, with normalized SAW amplitudes greater than 7×10^{-5}, the contact time is considerably reduced with an increase of the impact velocity. This is mainly due to the significant increase of the acoustic wave energy absorbed by the droplets. These results clearly confirm our prediction that, by breaking the droplet symmetry along both x and y axes, the contact time can be significantly reduced. However, the contact-time reduction achieved using this method is limited by

FIG. 8.   (a) Experimental results of normalized contact time as a function of SAW amplitude for droplets with initial diameters of 1.87, 2.04, and 2.22 mm. Impact velocity for all cases is kept constant at 1.7 m/s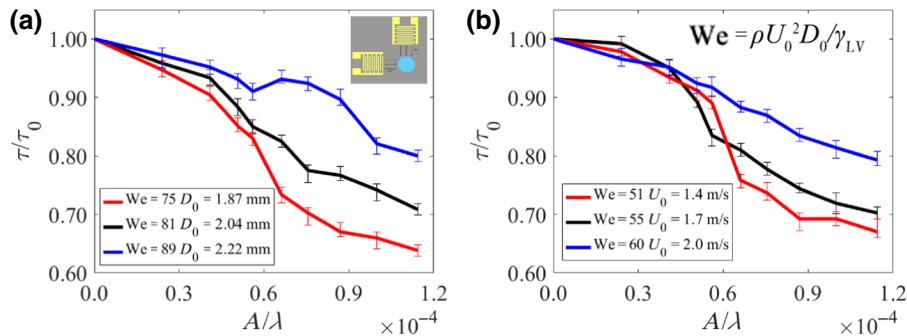. (b) Experimental results of normalized contact time as a function of SAW amplitude for droplets with impact velocities of 1.4, 1.7, and 2.0 m/s. Droplet initial diameter is kept constant at 1.87 mm. Error bars represent SD of contact time.

the power applied to the IDTs. Applying powers higher than 50 W could damage the SAW device and, at such higher powers, droplet tends to break up or splash during the spreading phase. Here, we only consider the cases in which complete rebounding is observed.

V. DISCUSSION

Overall, our results clearly indicate that the droplet impact dynamics can be modified and controlled using the thin-film-based SAW technique. The key features of the thin-film piezoelectric platform are its seamless, scalable, and localized generation of SAWs, which can then propagate across entire surfaces. Piezoelectric films can be deposited and applied locally on a component to generate vibrations, without the need for covering the whole surface with a piezoelectric film. The SAW direction and amplitude can also be controlled through electrode shapes and designs, and SAWs can also be generated wirelessly and remotely. Therefore, due to its high efficiency and wireless function, the SAW technique can be used in different engineering applications.

As shown in Fig. 4, a SAW can change the impact regime; thus, a potential application of this technology could be switching a nontextured surface to one that is water repellent in various structures, such as the surface of solar panels or vehicle (or airplane or train) windows. Additionally, for applications in which it is desirable to minimize the interaction between a solid and liquid to avoid surface erosion (for instance, wind-turbine blades), this method can effectively be used. Moreover, the ability to clean and remove the impacting liquid droplet makes it possible to fabricate anticontamination or antibacterial surfaces using this method [39,58,59]. The ability to reduce the contact time of the droplet can also be used to control heat transfer between a solid and liquid, or for deicing and anti-icing applications in airplane wings or wind-turbine surfaces. On the other hand, for spray-cooling applications, such as the spray cooling of nuclear reactors [60] and electronic components [63], it is desirable to control the contact time and area of the droplet with a high-temperature surface to regulate the heat-transfer rate, and the method we propose here could be suitable for such spray-cooling applications.

VI. CONCLUSION

Here, we study the bouncing behavior of a bouncing droplet under the influence of SAWs. Our experimental and numerical results show that, using this method, the droplet contact time can be significantly reduced on a solid surface without changing the solid surface's texture or geometry. The SAW can effectively reduce the contact time by up to 35% when a traveling SAW is applied to the droplet. We achieve both vertical and asymmetric rebounds

and a reduction of the contact time without fabricating textured surfaces. Moreover, our results show that by applying SAWs to the droplet, the impact regime can be modified, and droplet deposition on the surface can be effectively avoided by applying SAWs to an impacting droplet to achieve complete rebound from the surface. Simulation results show that the internal streaming patterns for both the droplet free impact and standing SAW cases are almost symmetrical. On the other hand, applying the traveling SAW creates an irregular flow field, which breaks the symmetry of internal streaming and can reduce the contact time. For the droplet free impact and standing SAW cases, the vortices that are created during the retract phase dissipate the kinetic energy more than that in the TSAW, leading to a longer contact time before droplet separation from the surface. Since SAWs can be generated remotely from a drop impact location and can be switched on and off, this concept allows the rebound properties of droplets, including contact time, bounce angle, and maximum spreading width, to be controlled, regardless of the impact point. Importantly, surface acoustic waves can be propagated across large areas of a surface of interest, which can be planar or curved and made of many different types of materials. The approach removes the need to texture or shape a surface to achieve a reduced droplet impact time. We, therefore, believe that SAW-based droplet impact modification offers a different paradigm for controlling droplet impact in applications such as anti-icing, self-cleaning, and antierosion.

APPENDIX A: EFFECT OF SAW DEVICE SUBSTRATE

To see the effect of the Rayleigh angle on the contact time of the droplet, here we compare the droplet impact dynamics on ZnO/Al and ZnO/Si SAW devices with the same wavelength. Table II lists the measured frequency of the fabricated ZnO/Al device. The SAW force [see Eq. (A1)] is applied to the liquid medium along the Rayleigh angle, and the ratio of the components of the SAW forces in x and z directions is equal to the attenuation coefficient ($F_{\mathrm{SAW}z}/F_{\mathrm{SAW}x} = \alpha_1$) [40]. As shown in Table II, due to lower sound velocity on the aluminum substrate, the Rayleigh angle is larger for Al-based SAW devices, and thus, α_1 is lower.

Consequently, the ratio of $F_{\mathrm{SAW}z}/F_{\mathrm{SAW}x}$ is lower for the ZnO/Al device compared with that for the ZnO/Si device due to a larger Rayleigh angle. Experimental results of

TABLE II. Resonant frequency, Rayleigh angle, SCA, advancing contact angle, receding contact angle, and CAH for the ZnO/Al SAW device. Contact angles are measured after surface treatment with CYTOP. The contact time is measured for a 3.56 μl droplet with an impact velocity of 1.41 m/s.

SAW Device	Resonant frequency (MHz)	Rayleigh angle (deg)	α_1	θ_s (deg)	θ_{adv} (deg)	θ_{rec} (deg)	$\Delta\theta = \theta_{adv} - \theta_{rec}$ (deg)
ZnO/Al	40.40	34.75	1.46	114 ± 2	114 ± 1	105 ± 1	9 ± 2

droplet contact time on the surface of ZnO/Al and ZnO/Si SAW devices as a function of SAW amplitude are illustrated in Fig. 9(a). From Fig. 9(a), we can see that, at lower SAW amplitudes, the contact time for the ZnO/Al SAW device is reduced by up to 10% compared with that on the ZnO/Al device, however, by increasing the SAW amplitude ($A/\lambda > 6 \times 10^{-5}$), the contact time starts to increase sharply. On the other hand, for the ZnO/Si device, the contact time is decreased by increasing the SAW amplitude. Snapshots of the impact show that, by applying the TSAW to the droplet, it moves a certain distance along the x direction during impingement. The transition along the x direction on the surface before separation, Δx, for both devices is compared in Fig. 9(b). At large SAW amplitudes, Δx is larger for the Al-based devices. These results can be explained by further analysis of the forces applied to the liquid. At the given time of t after the start of impingement, we analyze the forces along the x direction to gain a better understanding of droplet transition during impingement. Due to strain formed along the three-phase contact line for a droplet in motion on a solid surface, a significant viscous force resists droplet motion. Assuming the contact area is circular during impingement, the viscous resistive force, F_v, can be simplified as the liquid surface tension per unit length [17].

Additionally, as described in Sec. IV, another resistive force is formed due to the CAH along the TPCL. By assuming that the contact area is a complete circle during impingement, the tangential CAH resistive force, F_{CAH}, can be calculated by [61]

$$F_{CAH} = 24/\pi^3 \gamma_{LV} \delta (\cos\theta_{rec} - \cos\theta_{adv}), \quad (A1)$$

where δ is the base diameter [see Fig. 9(c)]. Newton's second law can be written in the x direction as

$$F_{SAW} \sin\theta_R - F_{CAH} - F_v = m dv_x/dt, \quad (A2)$$

where m is the liquid mass. A few ms before detachment, δ and the TPCL length are significantly reduced [see snapshots in Fig. 9(b)], and thus, both resistive forces are minimized. Therefore, the x component of the SAW force can overcome the resisting forces and drive the droplet along the x direction before the z component of the SAW force detaches the whole liquid droplet from the surface. The ZnO/Al SAW device has a lower attenuation constant, compared with that of the ZnO/Si SAW device. Thus, the

x component of the SAW force is higher, which can drive the droplet on the surface in the x direction at high SAW forces before complete detachment. This, in turn, leads to a change in the contact time for ZnO/Al SAW devices. Since this paper aims to investigate the contact-time reduction by
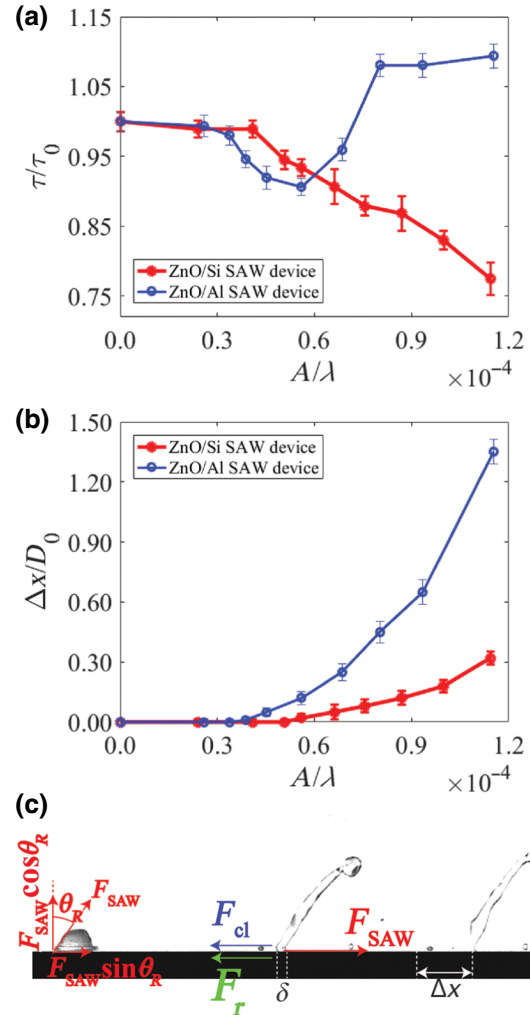
FIG. 9. (a) Experimental results of normalized contact time versus SAW amplitude for ZnO/Si and ZnO/Al SAW devices. For both devices, wavelength of the SAW is 64 μm, and a droplet with a volume of 3.56 μl impacts the surface with a velocity of 1.4 m/s. Contact time, τ, is normalized with the contact time of DFI case, τ_0, for each device. (b) Experimental results of transition distance in x direction before separation as a function of SAW amplitude. (c) Force analysis of impacting droplet.

using SAWs, we choose to continue our analysis with the ZnO/Si SAW devices.

APPENDIX B: EFFECT OF SAW FREQUENCY

To explore the effect of the resonant frequency on droplet impact dynamics, four different SAW devices are fabricated on the ZnO/Si surface by changing the structure of the IDTs. Details of the fabricated devices are presented in Table III.

To compare the effect of frequency on the dynamics of the impacting droplet, we normalize the SAW wavelength, λ, with the attenuation length of the SAW in the liquid medium, ζ [58]:

$$\zeta = \frac{\rho v_L{}^3}{4\pi^2 \omega^2 \left(\frac{4}{3}\mu + \mu'\right)}, \qquad \text{(B1)}$$

where μ and μ' are the shear and bulk viscosities of the fluid, respectively.

The effect of the SAW device resonant frequency on the contact time on the droplet is illustrated in Fig. B1. By increasing the wavelength (i.e., at a higher ζ/λ ratio), the SAW propagates longer distances within the liquid medium before significant attenuation. For the devices with a higher resonant frequency, the interaction volume between the SAW and liquid medium is decreased [59]. As a result, less momentum is transferred by SAWs to the liquid medium during impingement. As shown in Fig. 10, the SAW device with a resonant frequency of 110.82 MHz is not capable of significantly reducing the contact time. On the other hand, by effectively transferring the SAW momentum to the droplet during impingement, the contact time can be significantly reduced by SAW devices with lower resonant frequencies (i.e., 66.10 MHz and lower). However, for the SAW devices with resonant frequencies of 43.12 and 22.04 MHz, and at higher SAW amplitudes ($A/\lambda = 7 \times 10^{-5}$ for 43.12 MHz device and $A/\lambda = 7 \times 10^{-5}$ for 22.04 MHz device), the droplet impact regime can be changed from completely rebounding from the surface to breaking up. In this case, a few subunits are separated from the droplet during the retracting phase (see Fig. 10). The mechanism for droplet breakup can be explained by the attenuation length of the SAW in the liquid medium. At lower frequencies, the attenuation length in the liquid medium is higher, which leads to a higher SAW energy
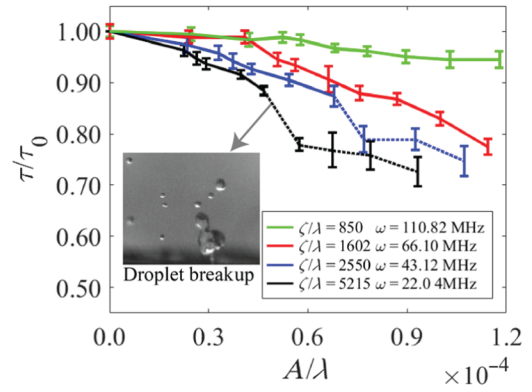

FIG. 10.   Experimental results of normalized contact time versus wave amplitude for SAW devices with different frequencies for a droplet with volume of 3.56 μl and impact velocity of 1.4 m/s impacting on the ZnO/Si SAW device surface with CYTOP surface treatment. Solid and dashed lines represent droplet rebounding and breakup regimes, respectively.

reaching the liquid-gas interface of the droplet. At larger amplitudes, this energy can overcome the surface tension of the droplet, and the droplet will break into smaller subunits. Considering the effect of frequency on the droplet behavior on the surface, we opt to use the SAW devices with a resonant frequency of 66.10 MHz to perform our studies.

APPENDIX C: DYNAMIC-CONTACT-ANGLE MODELING

As the droplet impingement phenomena in the presence of SAW are asymmetrical, to see the internal flow and recirculation inside the droplet, all numerical simulations are performed in three dimensions. A boundary condition is developed based on OpenFOAM, which calculates the dynamic contact angles based on the Bracke approach [63]:

$$\cos\theta_d = \cos\theta_s - (\cos\theta_s + 1)K_{\mathrm{DCA}}\mathrm{Ca}^{0.54}. \qquad \text{(C1)}$$

Here, the capillary number ($\mathrm{Ca} = \mu U_{\mathrm{CL}}/\gamma_{\mathrm{LV}}$) is defined based on the three-phase contact line velocity, U_{CL}, and K_{DCA} is set to 9.63 in all simulations. More details regarding the CLSVOF method used in simulations are presented in our previous works [51,52].

TABLE III.   Measured frequencies and calculated sound velocities and liquid attenuation lengths for ZnO/Si SAW devices.

Wavelength (μm)	Frequency (MHz)	$v_S(m/s)$	ζ/λ
36	110.82	3989.5	850
64	66.10	4230.4	1602
100	43.12	4312.0	2550
200	22.04	4407.5	5215

[1] K. Liu, X. Yao, and L. Jiang, Chem. recent developments in Bio-inspired special wettability, Soc. Rev. **39**, 3240 (2010).

[2] M. Cao, D. Guo, C. Yu, K. Li, M. Liu, and L. Jiang, Water-Repellent properties of superhydrophobic and lubricant-infused "slippery" surfaces: A brief study on the functions and applications, ACS Appl. Mater. Interfaces **8**, 3615 (2016).

[3] R. J. Daniello, N. E. Waterhouse, and J. P. Rothstein, Drag reduction in turbulent flows over superhydrophobic surfaces, Phys. Fluids **21,** 085103 (2009).

[4] Y. C. Jung and B. Bhushan, Dynamic effects of bouncing water droplets on superhydrophobic surfaces, Langmuir **24,** 6262 (2008).

[5] K. D. Esmeryan, A. H. Bressler, C. E. Castano, C. P. Fergusson, and R. Mohammadi, Rational strategy for the atmospheric icing prevention based on chemically functionalized carbon soot coatings, Appl. Surf. Sci. **390,** 452 (2016).

[6] L. Mishchenko, B. Hatton, V. Bahadur, J. A. Taylor, T. Krupenkin, and J. Aizenberg, Design of Ice-free nanostructured surfaces based on repulsion of impacting water droplets, ACS Nano **4,** 7699 (2010).

[7] C. Clanet, C. Béguin, D. Richard, and D. Quéré, Maximal deformation of an impacting drop, J. Fluid Mech. **517,** 199 (2004).

[8] J. Eggers, M. A. Fontelos, C. Josserand, and S. Zaleski, Drop dynamics after impact on a solid wall: Theory and simulations, Phys. Fluids **22,** 062101 (2010).

[9] R. Gupta, V. Vaikuntanathan, and D. Sivakumar, Superhydrophobic qualities of an aluminum surface coated with hydrophobic solution NeverWet, Colloids Surf. A Physicochem. Eng. Asp. **500,** 45 (2016).

[10] Z. Li, Q. Kong, X. Ma, D. Zang, X. Guan, and X. Ren, Dynamic effects and adhesion of water droplet impact on hydrophobic surfaces: Bouncing or sticking, Nanoscale **9,** 8249 (2017).

[11] M. Abolghasemibizaki and R. Mohammadi, Droplet impact on superhydrophobic surfaces fully decorated with cylindrical macrotextures, J. Colloid Interface Sci. **509,** 422 (2018).

[12] B. Ding, H. Wang, X. Zhu, R. Chen, and Q. Liao, Int. water droplet impact on superhydrophobic surfaces with various inclinations and supercooling degrees, J. Heat Mass Transf. **138,** 844 (2019).

[13] Lord Rayleigh, On the capillary phenomena of jets, Proc. R. Soc. London **29,** 71 (1879).

[14] J. C. Bird, R. Dhiman, H. M. Kwon, and K. K. Varanasi, Reducing the contact time of a bouncing drop, Nature **503,** 385 (2013).

[15] A. Gauthier, S. Symon, C. Clanet, and D. Quéré, Water impacting on superhydrophobic macrotextures, Nat. Commun. **6,** 8001 (2015).

[16] Y. Shen, J. Tao, H. Tao, S. Chen, L. Pan, and T. Wang, Approaching the theoretical contact time of a bouncing droplet on the rational macrostructured superhydrophobic surfaces, Appl. Phys. Lett. **107,** 111604 (2015).

[17] H. Li, W. Fang, Y. Li, Q. Yang, M. Li, Q. Li, X. Q. Feng, and Y. Song, Spontaneous droplets gyrating via asymmetric self-splitting on heterogeneous surfaces, Nat. Commun. **10,** 950 (2019).

[18] Y. C. Jung and B. Bhushan, Wetting transition of water droplets on superhydrophobic patterned surfaces, Scr. Mater. **57,** 1057 (2007).

[19] V. Fink, X. Cai, A. Stroh, R. Bernard, J. Kriegseis, B. Frohnapfel, H. Marschall, and M. Wörner, Drop bouncing by micro-grooves, Int. J. Heat Fluid Flow **70,** 271 (2018).

[20] V. Vaikuntanathan and D. Sivakumar, Maximum spreading of liquid drops impacting on groove-textured surfaces: Effect of surface texture, Langmuir **32,** 2399 (2016).

[21] M. Song, Z. Liu, Y. Ma, Z. Dong, Y. Wang, and L. Jiang, Reducing the contact time using macro anisotropic superhydrophobic surfaces-effect of parallel wire spacing on the drop impact, NPG Asia Mater. **9,** e415 (2017).

[22] C. Guo, D. Zhao, Y. Sun, M. Wang, and Y. Liu, Droplet impact on anisotropic superhydrophobic surfaces, Langmuir **34,** 3533 (2018).

[23] C. Guo, D. Maynes, J. Crockett, and D. Zhao, Heat transfer to bouncing droplets on superhydrophobic surfaces, Int. J. Heat Mass Transf. **137,** 857 (2019).

[24] B. A. Malouin, N. A. Koratkar, A. H. Hirsa, and Z. Wang, Directed rebounding of droplets by microscale surface roughness gradients, Appl. Phys. Lett. **96,** 1 (2010).

[25] Y. Liu, L. Moevius, X. Xu, T. Qian, J. M. Yeomans, and Z. Wang, Pancake bouncing on superhydrophobic surfaces, Nat. Phys. **10,** 515 (2014).

[26] Y. Liu, G. Whyman, E. Bormashenko, C. Hao, and Z. Wang, Controlling drop bouncing using surfaces with gradient features, Appl. Phys. Lett. **107,** 51604 (2015).

[27] J. Song, M. Gao, C. Zhao, Y. Lu, L. Huang, X. Liu, C. J. Carmalt, X. Deng, and I. P. Parkin, Large-Area fabrication of droplet pancake bouncing surface and control of bouncing state, ACS Nano **11,** 41 (2017).

[28] Y. Liu, M. Andrew, J. Li, J. M. Yeomans, and Z. Wang, Symmetry breaking in drop bouncing on curved surfaces, Nat. Commun. **6,** 10034 (2015).

[29] S. Jowkar and M. R. Morad, Water drop impact on a semicylindrical convex Hot surface for a diameter ratio of unity, Exp. Therm. Fluid Sci. **106,** 68 (2019).

[30] S. Chen and V. Bertola, Drop impact on spherical soft surfaces, Phys. Fluids **29,** 082106 (2017).

[31] P. B. Weisensee, J. Ma, Y. H. Shin, J. Tian, Y. Chang, W. P. King, and N. Miljkovic, Droplet impact on vibrating superhydrophobic surfaces, Phys. Rev. Fluids **2,** 103601 (2017).

[32] L. Y. Yeo and J. R. Friend, Ultrafast microfluidics using surface acoustic waves, Biomicrofluidics **3,** 012002 (2009).

[33] J. Zhou, H. F. Pang, L. Garcia-Gancedo, E. Iborra, M. Clement, M. De Miguel-Ramos, H. Jin, J. K. Luo, S. Smith, S. R. Dong, D. M. Wang, and Y. Q. Fu, Discrete microfluidics based on aluminum nitride surface acoustic wave devices, Microfluid. Nanofluidics **18,** 537 (2015).

[34] A. Zhang, Y. Zha, and J. Zhang, A surface acoustic wave micropump to pump fluids from a droplet into a closed microchannel using evaporation and capillary effects, Cit. AIP Adv. **4,** 127144 (2014).

[35] Z. Wang and J. Zhe, Recent advances in particle and droplet manipulation for Lab-on-a-chip devices based on surface acoustic waves, Lab Chip **11,** 1280 (2011).

[36] Y. J. Guo, A. P. Dennison, Y. Li, J. Luo, X. T. Zu, C. L. Mackay, P. Langridge-Smith, A. J. Walton, and Y. Q. Fu, Nebulization of water/glycerol droplets generated by ZnO/Si surface acoustic wave devices, Microfluid. Nanofluidics **19,** 273 (2015).

[37] T. H. Bui, V. Nguyen, S. Vollebregt, B. Morana, H. van Zeijl, T. Chu Duc, and P. M. Sarro, Effect of droplet shrinking on surface acoustic wave response in microfluidic applications, Appl. Surf. Sci. **426,** 253 (2017).

[38] M. Baudoin, P. Brunet, O. B. Matar, and E. Herth, Low power sessile droplets actuation via modulated surface acoustic waves, Cit. Appl. Phys. Lett. **100,** 154102 (2012).

[39] Y. Q. Fu, J. K. Luo, N. T. Nguyen, A. J. Walton, A. J. Flewitt, X. Zu, Y. Li, G. McHale, A. Matthews, E. Iborra, H. Du, and W. I. Milne, Advances in piezoelectric thin films for acoustic biosensors, acoustofluidics and Lab-on-chip applications, Prog. Mater. Sci. **89,** 31 (2017).

[40] S. Shiokawa, Y. Matsui, and T. Ueda, Study on Saw streaming and Its application to fluid devices, Jpn. J. Appl. Phys. **29,** 137 (1990).

[41] S. K. R. S. Sankaranarayanan, S. Cular, V. R. Bhethanabotla, and B. Joseph, Flow induced by acoustic streaming on surface-acoustic-wave devices and Its application in biofouling removal: A computational study and comparisons to experiment, phys. Rev. E - stat. nonlinear, Soft Matter Phys. **77,** 1 (2008).

[42] M. Alghane, Y. Q. Fu, B. X. Chen, Y. Li, M. P. Y. Desmulliez, and A. J. Walton, Frequency effect on streaming phenomenon induced by Rayleigh surface acoustic wave in microdroplets, J. Appl. Phys. **112,** 084902 (2012).

[43] M. Aminzadeh, A. Maleki, B. Firoozabadi, and H. Afshin, On the motion of newtonian and Non-newtonian liquid drops, Sci. Iran. **19,** 1265 (2012).

[44] Š Šikalo, H. D. Wilhelm, I. V. Roisman, S. Jakirlić, and C. Tropea, Dynamic contact angle of spreading droplets: Experiments and simulations, Phys. Fluids **17,** 1 (2005).

[45] M. Sussman and E. G. Puckett, A coupled level Set and volume-of-fluid method for computing 3D and axisymmetric incompressible Two-phase flows, J. Comput. Phys. **162,** 301 (2000).

[46] S. Afkhami, S. Zaleski, and M. Bussmann, A mesh-dependent model for applying dynamic contact angles to VOF simulations, J. Comput. Phys. **228,** 5370 (2009).

[47] S. Yun, Bouncing of an ellipsoidal drop on a superhydrophobic surface, Sci. Rep. **7,** 17699 (2017).

[48] D. Richard, C. Clanet, and D. Quéré, Surface phenomena: Contact time of a bouncing drop, Nature **417,** 811 (2002).

[49] Y. Shen, J. Tao, H. Tao, S. Chen, L. Pan, and T. Wang, Relationship between wetting hysteresis and contact time of a bouncing droplet on hydrophobic surfaces, ACS Appl. Mater. Interfaces **7,** 20972 (2015).

[50] M. Pasandideh-Fard, Y. M. Qiao, S. Chandra, and J. Mostaghimi, Capillary effects during droplet impact on a solid surface, Phys. Fluids **8,** 650 (1996).

[51] M. Jangi, J. T. Luo, R. Tao, J. Reboud, R. Wilson, J. M. Cooper, D. Gibson, and Y. Q. Fu, Oncentrated vertical jetting mechanism for isotropically focused Zno/Si surface acoustic waves, Int. J. Multiph. Flow **114,** 1 (2019).

[52] M. H. Biroun, M. T. Rahmati, M. Jangi, R. Tao, B. X. Chen, and Y. Q. Fu, Computational and experimental analysis of droplet transportation/jetting behaviours driven by thin film surface acoustic waves, Sens. Actuators, A Phys. **299,** 111624 (2019).

[53] H. Ma, C. Liu, X. Li, H. Huang, and J. Dong, Deformation characteristics and energy conversion during droplet impact on a water surface, Phys. Fluids **31,** 062108 (2019).

[54] A. Bisighini, G. E. Cossali, C. Tropea, and I. V. Roisman, Crater evolution after the impact of a drop onto a semi-infinite liquid target, Phys. Rev. E **82,** 036319 (2010).

[55] N. Erkan, Full-Field spreading velocity measurement inside droplets impinging on a Dry solid-heated surface, Exp. Fluids **60,** 88 (2019).

[56] J. B. Lee, D. Derome, A. Dolatabadi, and J. Carmeliet, Energy budget of liquid drop impact at maximum spreading: Numerical simulations and experiments, Langmuir **32,** 1279 (2016).

[57] A. K. Saha, K. Muralidhar, and G. Biswas, Vortex structures and kinetic energy budget in Two-dimensional flow past a square cylinder, Comput. Fluids **29,** 669 (2000).

[58] W. Connacher, N. Zhang, A. Huang, J. Mei, S. Zhang, T. Gopesh, and J. Friend, Micro/nano acoustofluidics: Materials, phenomena, design, devices, and applications, Lab Chip **18,** 1952 (2018).

[59] Y. J. Guo, H. B. Lv, Y. F. Li, X. L. He, J. Zhou, J. K. Luo, X. T. Zu, A. J. Walton, and Y. Q. Fu, High frequency microfluidic performance of LiNbO$_3$ and ZnO surface acoustic wave devices, J. Appl. Phys. **116** (2014).

[60] N. Fries and M. Dreyer, The transition from inertial to viscous flow in capillary rise, J. Colloid Interface Sci. **327,** 125 (2008).

[61] R. Tao, G. McHale, J. Reboud, J. M. Cooper, H. Torun, J. Luo, J. Luo, X. Yang, J. Zhou, P. Canyelles-Pericas, Q. Wu, and Y. Fu, Hierarchical nanotexturing enables acoustofluidics on slippery yet sticky, flexible surfaces, Nano Lett. **20,** 3263 (2020).

[62] See the Supplemental Material at http://link.aps.org/supplemental/10.1103/PhysRevApplied.14.024029 for experimental movies of DI water droplet impact on SAW device.

[63] M. Bracke, F. De Voeght, P. Joos, in Trends in Colloid and Interface Science III, edited by P. Bothorel and E. J. Dufourc (1989), Vol **79.**